1   **Revision 1**

2   **Raman Spectroscopic Investigation of Selected Natural Uranyl Sulfate Minerals**

3   **Tyler L. Spano[1], Travis A. Olds[2], Marshall McDonnell[3], Robert Smith[3], and Ashley E.**
4   **Shields[1]**

5   [1]*Nuclear Nonproliferation Division, Oak Ridge National Laboratory, 1 Bethel Valley Road, Oak*
6   *Ridge, Tennessee, 37831, USA*

7   [2]*Carnegie Museum of Natural History, 4400 Forbes Avenue, Pittsburgh, Pennsylvania, 15213,*
8   *USA*

9   [3]*Computer Science and Mathematics Division, Oak Ridge National Laboratory, 1 Bethel Valley*
10   *Road, Oak Ridge, Tennessee, 37831, USA*

11   **Abstract**

12   Uranyl sulfates are important constituents of uranium ores and represent a significant fraction of

13   U(VI) minerals discovered in recent years owing to their propensity to form in mine tailings and

14   legacy sites related to uranium exploration. Recently, we surveyed all published Raman spectra

15   for uranium minerals and found significantly less easily accessible data available for uranyl

16   sulfates relative to other groups of uranium minerals. In that work we described average spectra

17   for groups of uranyl minerals to understand common vibrational spectroscopic features

18   attributable to similarities in oxyanion chemistry among U(VI) minerals, but only data for three

19   uranyl sulfate minerals were included in the study. The present work reports on Raman spectra

20   collected for 18 additional uranyl sulfate minerals. To better understand underlying structural

21   and chemical features that give rise to spectroscopic observables, we relate differences in

22   structural topology, charge balancing cations, and locality of origin to features observed in the

23   Raman spectra of selected natural uranyl sulfates.

24   **Keywords:** uranyl sulfates, Raman spectroscopy, U(VI) minerals

Introduction

25

26   Accurate, nondestructive identification of uranium-bearing compounds is of critical

27   interest in the fields of nuclear forensics, environmental remediation, and resource exploration.

28   Uranyl sulfate minerals are important constituents of uranium ore deposits, occurring as

29   weathering products via oxidation-hydration alteration of primary uranium oxides such as

30   uraninite (Plášil, 2014). The propensity for uranyl sulfate occurrences are due in part to the

31   interaction of decomposing primary sulfide phases, resulting in low-pH, aqueous complexes of

32   UO_2^{2+} and SO_4^{2-} (Finch and Murakami, 1999; Krivovichev and Plášil, 2013). Analogously,

33   sulfuric acid is commonly employed during uranium extraction and milling operations (Seidel,

34   1981; Sharifironizi et al., 2016), resulting in a diverse population of technogenic uranyl sulfate

35   phases (Guettaf et al., 2009; Ling et al., 2010).

36   Systematic descriptions of both naturally occurring (Burns et al., 2003; Finch and

37   Murakami, 1999; Gurzhiy and Plášil, 2019; Krivovichev and Plášil, 2013; Tyumentseva et al.,

38   2019) and technogenic (Kohlgruber et al., 2022; Smith et al., 2018; Tyumentseva et al., 2019)

39   uranyl sulfates species are provided elsewhere. Briefly, uranyl sulfate minerals are composed of

40   U(VI) in pentagonal bipyramidal coordination, further linked through edge- and vertex-shared

41   SO_4 tetrahedra, forming a topologically diverse group of minerals. Currently, 46 uranyl sulfate

42   minerals are recognized by the International Mineralogical Association, making sulfates the most

43   numerous group of uranyl minerals. Linkages between U(VI) and S(VI) polyhedra are typically

44   monodentate with few exceptions (Burns et al., 2003; Gurzhiy and Plášil, 2019). Uranyl sulfate

45   minerals predominantly form sheet-like 2-D structures, however, some are known to crystallize

46   with infinite chain topologies, and few structures with isolated clusters of polyhedra are reported.

47   In addition to classification based upon structure type, uranyl sulfates may also be categorized by

48 relations between their overall bond topologies with previously described species (Burns, 2005;

49 Lussier et al., 2016). Gurzhiy and Plášil (Gurzhiy and Plášil, 2019) describe eight categories of

50 structural topologies in which uranyl sulfate minerals may be grouped, including the zippeite

51 (Burns et al., 2003), leydetite (Plášil et al., 2013b), phosphuranylite (Demartin et al., 1991), and

52 mathesiusite (Plášil et al., 2014c) topologies, as well as isolated clusters, chains of polyhedra,

53 dense chains of polyhedra, and rare layers (Gurzhiy and Plášil, 2019).

54   To elucidate the relationships between structural attributes and observable spectroscopic

55 features, here we discuss in detail the Raman spectra of uranyl sulfate minerals and the

56 underlying crystallographic features from which they originate. This work focuses on mineral

57 species possessing the zippeite, mathesiusite, and phosphuranylite anion topologies and members

58 of the uranyl sulfates that are composed of isolated clusters, chains of polyhedra, and dense

59 chains of polyhedra, as delineated by Gurzhiy and Plášil (Gurzhiy and Plášil, 2019). First,

60 common features are examined in the spectra of all uranyl sulfate minerals, then we discuss

61 average spectra calculated for groups of uranyl sulfate minerals based on structure type (and

62 anion topology). As a means towards understanding potential crystal–chemical influences that

63 charge balancing cations may have on observable spectroscopic features, we examine differences

64 between the spectra of individual mineral species belonging to a given structural group. Finally,

65 we explore the possible influence of sample origin (locality) on spectroscopic observations on

66 minerals of the same species.

Materials and Methods

68   Uranyl sulfate minerals investigated in this work are summarized in Table 1 and include

69 Co-rich zippeite (Burns et al., 2003), Zn-rich zippeite (Burns et al., 2003), ammoniozippeite

70 (Kampf et al., 2018b), natrozippeite (Burns et al., 2003), uranopilite (Burns, 2001),

71   ammoniomathesiusite (Kampf et al., 2019c), johannite (Donnay, 1955; Mereiter, 1982),

72   marécottite (Brugger et al., 2003; Burns et al., 2003), lussierite (Kampf et al., 2019b),

73   zincorietveldite (Kampf et al., 2023), navrotskyite (Miyawaki et al., 2019), fermiite (Kampf et

74   al., 2015b), belakovskiite (Kampf et al., 2014), plášilite (Kampf et al., 2015a), feynmanite

75   (Kampf et al., 2019a), bluelizardite (Plášil et al., 2014b), meisserite (Plášil et al., 2013a), and

76   rabejacite (Plášil et al., 2014a). Crystalline samples of each mineral listed in Table 1 were

77   extracted from matrix as aggregates of crystalline material with a tungsten fine-tipped needle

78   (0.6 μm). The size of the crystals varied from finely powdered (< 1 μm crystallite size, e.g.

79   zippeites D and E) to macroscopically crystalline (~20 μm and larger) for the remaining phases.

80   In some instances, the extracted aggregates contained adhering gypsum or asphaltum matrix.

81   Care was taken to ensure that adhering or other associated phases did not interfere with the

82   measured data, and that the spectra presented are phase pure. For each uranyl sulfate mineral

83   species investigated in this work, Raman spectra were collected using a Renishaw InVia micro-

84   Raman spectrometer with a 785 nm excitation wavelength equipped with a 1200 lines/mm

85   diffraction grating, resulting in a resolution of ~2.5–3.1 cm^{-1} and an approximate power density

86   of 100 W/cm^2 based upon laser power (10 mW) and spot size (~1 μm^2). Data were collected as

87   20 accumulations of 10 s of data in the range of 50–1250 cm^{-1}. Raw data were imported into

88   OriginPro (2021) for analysis. To facilitate comparing spectra for minerals with varying Raman

89   signal intensity, each data set was normalized by dividing each data point by the integrated total

90   counts over the spectral range of interest.

91   **Results and Discussion**

92   **Average Uranyl Sulfate Spectrum and Average Spectra Based on Structure Type**

93   To understand common spectral features among uranyl minerals and technogenic phases

94   with similar chemical compositions, we recently determined average spectra for groups of uranyl

95   minerals based on secondary oxyanion chemistry (e.g., structural components in addition to U

96   and O) to apply as features for machine learning applications (McDonnell et al., 2022; Spano et

97   al., 2023). In addition, we used principal component analyses combined with partial least squares

98   regression to reveal additional underlying chemical and structural features that could contribute

99   to optical vibrational spectroscopic observables and potentially lead to identification of unknown

100   U-rich materials. When calculating the average spectrum for uranyl sulfate minerals in that work,

101   we identified a lack of readily available Raman spectra for this group. Furthermore, the average

102   uranyl sulfate spectrum we reported notably lacked contributions from zippeite group minerals.

103   To better understand common characteristics of the Raman spectra of uranyl sulfates, the present

104   study details the new average spectrum for uranyl sulfate minerals, which contains the species

105   included in Table 1 in addition to the mineral spectra already included in CURIES (Compendium

106   of Uranium Raman and Infrared Experimental Spectra) (Spano et al., 2023). A comparison of the

107   previously published and new average spectra is shown in Figure 1.

108   The addition of new data sets to the average uranyl sulfate spectrum reveals several

109   notable features. At low energy, 3 bands of spectral intensity are observed, located at ~290, 321,

110   and 354 cm^{-1}. The features at ~290 and 354 cm^{-1} were present in the initial average spectrum but

111   are fully resolved in the updated average data set. A shoulder peak located at 396 cm^{-1} is now

112   visible in the updated average spectrum, coupled with an increase in intensity of the apparent

113   vibrational mode centered at 423 cm^{-1}. A diffuse, low-intensity band located at ~490 cm^{-1} in the

114   initial average spectrum is replaced by a broad apparent doublet of modes between 450 and 515

115   cm^{-1} in the updated version, attributable to v_2 SO_4^{2-} bending in zippeite group species. Several

116   low intensity features are observed in the range of 590–680 cm^{-1} in the updated spectrum, likely

117   related to contributions from the v_4 SO$_4^{2-}$ bending vibrational mode present in zippeite group

118   uranyl sulfates. Most notably, the v_1 UO$_2^{2+}$ symmetric stretching vibrational mode, previously

119   centered at ~837 cm^{-1}, is replaced by an apparent quartet of modes between 780–871 cm^{-1},

120   which corresponds to U-O$_{yl}$ bond lengths between 1.83-1.74 Å based on the relationship between

121   bond length and v_1 UO$_2^{2+}$ frequency described by Bartlett and Cooney (1989). This additional

122   complexity is certainly attributable to the inclusion of spectra for more diverse uranyl sulfate

123   species with cluster, chain, and sheet structures now represented in the updated average uranyl

124   sulfate spectrum. 2 additional low-intensity bands centered at 916 and 936 cm^{-1} are visible in the

125   updated average spectrum. As was observed for the uranyl symmetric stretching vibrational

126   mode, an increase in relative intensity and complexity is seen in the SO$_4^{2-}$ region of the updated

127   average spectra, with several low energy shoulders associated with an apparent triad of modes

128   between 985 and 1030 cm^{-1} attributable to symmetric and/or antisymmetric SO$_4^{2-}$ stretching

129   vibrations. Although visible in the initial average spectrum for uranyl sulfates, the feature located

130   at ~1045 cm^{-1} is better resolved in the updated data. Finally, the broad peak centered at ~1093

131   cm^{-1} in the older data set is replaced by 2 spectral features centered at ~1075 and 1090 cm^{-1},

132   likely also related to SO$_4^{2-}$ stretching vibrations (Frost et al., 2005a). These spectroscopic details

133   resulting from inclusion of additional uranyl sulfate spectra in CURIES will aid in determining

134   features associated with this oxyanion chemistry for machine learning applications.

135   Beyond investigating average uranyl sulfate mineral spectra for all species in this

136   oxyanion group, this study also determines the average spectra of groups of uranyl sulfates based

137   on their structure type. This information can provide insight into spectroscopic features imparted

138   by similarities in underlying structure or topology with a similar goal of using these features to

139   train machine learning models to recognize uranyl sulfates from Raman spectra. Figure 2 shows

140   average spectra calculated for members of the zippeite and phosphuranylite groups and average

141   spectra for uranyl sulfates composed of chains of polyhedra and isolated clusters, with details of

142   assignments provided in Table 2. Features of the uranyl region are discussed in detail elsewhere

143   (Lu et al., 2018), so this study focuses instead on interpretation of spectroscopic features that

144   originate from S–O and equatorial U–O (U-O$_{eq}$) vibrational modes.

145   The average spectrum of zippeite group sulfates is distinguished by a band centered at

146   157 cm^{-1}, an apparent quartet of modes between ~380 and 550 cm^{-1}, a doublet with a high-

147   energy shoulder in the uranyl region (~760–890 cm^{-1}), an apparent doublet of modes between

148   ~1000 and 1050 cm^{-1}, and a low-intensity peak centered at ~1090 cm^{-1}. The peak at 157 cm^{-1},

149   likely attributable to U-Oeq modes (Plášil et al., 2010) appears to be a unique feature of zippeite

150   group uranyl sulfates. Similarly, the spectral features observed between 380 and 550 cm^{-1} in the

151   average zippeite group spectrum appears to be signatory of this structure type relative to other

152   uranyl sulfates examined in this work, which are attributable to the overlap of v_2 UO$_2^{2+}$, U–O$_{eq}$,

153   and v_3 SO$_4^{2-}$ modes of members of this group (discussed in the next section). Moving to the peak

154   centered at 1,015 cm^{-1} originating from the v_1 SO$_4^{2-}$ symmetric stretching mode, we note that the

155   location of this vibration occurs at significantly higher energy (~15 cm^{-1} higher) relative to the

156   analogous mode in the average spectra of chains of polyhedra and isolated clusters. Likewise,

157   this is at lower energy than the appearance of the v_1 SO$_4^{2-}$ in the average spectrum of

158   phosphuranylite group uranyl sulfates. Lower frequency v_1 SO$_4^{2-}$ vibrations in the zippeite group

159   (relative to phosphuranylite species) may result from coordination effects—every sulfate group

160   in the zippeite topology shares vertices with a U coordination polyhedra, perhaps limiting the

161   extent of atomic motion.

162   The average spectrum for phosphuranylite group uranyl sulfates is characterized by low

163   intensity spectral features centered at ~205, 245, 450, 625, 880, and 1145 cm^{-1}. Additionally, an

164   intermediate intensity band is located at ~1045cm^{-1}, and an apparent doublet of modes appears

165   between 1070 and 1115 cm^{-1}. The bands located at 205 and 245 cm^{-1} in the average

166   phosphuranylite spectrum are likely attributable to v_2 U–O–U bending modes based on

167   assignments for feynmanite by Kampf et al. (2019a). Similarly, the weak bands at ~450 and 625

168   cm^{-1} may be attributable to doubly and triply degenerate v_2 and v_4 SO$_4^{2-}$ bending modes,

169   respectively (Kampf et al., 2018a). Contributions from the v_1 SO$_4^{2-}$ symmetric stretching

170   vibration are observed at ~1045 cm^{-1}, with an additional doublet of bands belonging to v_3 SO$_4^{2-}$

171   vibrations present between 1075 and 1115 cm^{-1}. The higher energy appearance of the v_1 and v_3

172   SO$_4^{2-}$ modes in the average Raman spectrum of phosphuranylite group uranyl sulfates may be

173   used to distinguish species of this group from zippeite-type structures, where these same bands

174   are present at ~1015 and 1040 cm^{-1}.

175   The low-energy region of the average spectrum calculated for uranyl sulfates possessing

176   structures based on chains of polyhedra (rietveldite, navrotskyite, fermiite, and meisserite) is

177   characterized by a medium-intensity band centered at 230 cm^{-1} and several regions of low-

178   intensity spectral features between ~320, 410–475, and 585–675 cm^{-1}. A distinct band centered

179   at 230 cm^{-1} is attributable to v_2 U–O–U based on assignments for fermiite (Kampf et al., 2015b).

180   The high-energy region (~900 cm^{-1} and above) is the most complex for this average spectrum

181   relative to other groups of uranyl sulfate minerals. The complexity seems to originate largely

182   from contributions of the fermiite and meisserite spectra to the average, which may be

183   attributable to the large number of crystallographically distinct SO$_4^{2-}$ groups (4) in these species

184   relative to other uranyl sulfates composed of chains of polyhedra.

185   The average spectrum for uranyl sulfate minerals containing isolated clusters is

186   characterized by several areas of diffuse, low-intensity bands in the regions of 150–250, 415–

187   475, and 600–660 cm^{-1}. An additional low-intensity feature is observed at ~935 cm^{-1} with an

188   apparent triplet of modes centered at 1000 cm^{-1}, which distinguishes the average spectrum of

189   isolated cluster-type species from other uranyl sulfates. Although the position of the 1000 cm^{-1}

190   triplet of modes is centered similarly to the v_1 and v_3 SO_4^{2-} modes in the average spectrum

191   calculated for uranyl sulfates possessing chains of polyhedra, the feature at 1000 cm^{-1} in the

192   average spectrum for isolated cluster uranyl sulfates is significantly broader than the analogous

193   1-D chain spectral peak.

194   **Zippeite Group**

195   Individual Raman spectra collected for uranyl sulfate minerals belonging to the zippeite

196   group (Figure 3) are shown in Figures 4a–c. Although the crystallographic symmetry and

197   chemical composition of zippeite group minerals are highly variable, some exhibit extensive

198   solid solution and they all contain topologically identical sheet structures. Minerals belonging to

199   this group are characterized by infinite sheets of uranyl pentagonal bipyramids linked through

200   sharing of equatorial edges and vertices (Figure 3a). Each uranyl pentagonal bipyramid shares

201   vertices with two sulfate tetrahedra, serving to form the extended sheet topology with a

202   characteristic U:S ratio of 2:1. A notable feature present in the Raman spectra of zippeite group

203   minerals is variability in the position of the v_1 UO_2^{2+} symmetric stretching vibrational mode

204   (Plášil et al., 2010). Natrozippeite spectra are characterized by a mode centered at 840 cm^{-1},

205   whereas Zn-rich zippeite, Co-rich zippeite, and marécottite possess a lower energy uranyl peak,

206   centered at approximately 810 cm^{-1} (Figure 4b). A low-intensity peak is also observed around

207   810 cm^{-1} in some of the spectra collected for natrozippeite, which we initially hypothesized

208   could result from either an admixture or solid solution with other zippeite group phases.

209   However, Plášil et al. note that significant polarization dependance is possible when collecting

210   Raman spectra for zippeite. Resultingly, we believe this contribution originates a slight shift in

211   the position of v_1 UO_2^{2+} arising from differences in the orientation of individual crystallites in the

212   sample we analyzed (Plášil et al., 2010) . Both ammoniozippeite and rabejacite spectra show

213   uranyl vibrational mode positions that are distinct from other zippeite group phases, with broad,

214   relatively low intensity vibrational modes centered at ~831 cm^{1-} for ammoniozippeite and 852

215   cm^{-1} for rabejacite (Figure 4b). Differences are also observed in the v_1 SO_4^{2-} vibrational mode

216   amongst zippeite group species. Like observations of the v_1 UO_2^{2+}, Zn-rich zippeite, Co-rich

217   zippeite, and marécottite have similarly positioned v_1 SO_4^{2-} modes, centered at approximately

218   1015 cm^{-1} however, despite the distinct uranyl band observed in ammoniozippeite, the v_1 SO_4^{2-}

219   symmetric sulfate stretching mode also appears here (Plášil et al., 2010). Natrozippeite spectra

220   show a lower energy v_1 SO_4^{2-} centered at ~1010 cm^{-1}. Likewise, the v_1 SO_4^{2-} mode in rabejacite

221   is found at higher energy, ~1035 cm^{-1}. The position of the v_3 SO_4^{2-} mode is also variable in the

222   zippeite group. In general, the position of this mode is centered at ~1090 cm^{-1} in natrozippeite,

223   although additional spectral features are present at higher energy in some specimens examined,

224   which may obscure the appearance of this mode. The variability in the background of

225   natrozippeite spectra at high energy may be attributable to different host rock species for the

226   samples examined related to the varied localities from which they originate. Further differences

227   between natrozippeite spectra from different localities will be discussed in a later section. Zn-

228   rich zippeite, Co-rich zippeite, ammoniozippeite, and marécottite have similar spectral positions

229   for the v_3 SO_4^{2-}, with this mode appearing at ~1095 cm^{-1} and likely arising from structural

230   similarities between these zippeite species. The v_3 SO_4^{2-} mode in rabejacite is found at higher

231 energy, centered at ~1115 cm^{-1}. Significant complexity is observed in the low-energy region of

232 zippeite group uranyl sulfate spectra.

233   In general for zippeite group species, the v_1 UO$_2^{2+}$ mode appears at approximately

234 275 cm^{-1}, equatorial (U–O$_{eq}$) modes at ~350–375 cm^{-1}, and v_3 SO$_4^{2-}$ modes at approximately

235 ~400–500 cm^{-1}, all based on assignments from Frost et al. (2005a). The low-energy region of

236 spectra collected for zippeite group uranyl sulfates is shown in Figure 4c. In general, spectral

237 features of Zn-rich zippeite coincide with low-wavenumber modes for Co-rich zippeite and

238 marécottite. Ammoniozippeite, natrozippeite, and rabejacite modes appear to be shifted relative

239 to these species. However, natrozippeite shows 2 bands of intermediate intensity at 191 and 396

240 cm^{-1}, ammoniozippeite has similar spectral feautres centered at 150 and 405 cm^{-1}, and in

241 rabejacite, these are found at 165 and 455 cm^{-1}. Although no assignments are available for

242 modes below 200 cm^{-1} from Frost et al., these authors assign modes between 400 and 500 cm^{-1}

243 to U–O equatorial vibrations. The observed spectral shifts in this region likely originate from a

244 combination of various lattice vibrations and differences in equatorial O bond strengths imparted

245 by interactions with different interstitial charge balancing cations.

246 **Phosphuranylite Group**

247   Johannite, plášilite, and feynmanite (Figure 5a) all contain sheets composed of dimers of

248 uranyl pentagonal bipyramids interlinked through sharing of vertices with uranyl sulfate

249 tetrahedra (Figure 5b). Structural differences between these species arise from changes in the

250 manner in which uranyl pentagonal dimeric units are interlinked via sulfate tetrahedra and, in

251 particular, the direction in which apical O associated with SO$_4^{2-}$ tetrahedra are pointing. These

252 distinct local directionalities are manifested in unique uranyl and sulfate vibrational mode

253 frequencies within the Raman spectra of these species (see Figure 6). Variations in the position

254   of the v_1 UO_2^{2+} mode are observed in the spectra of these species, with peaks centered at ~830,

255   845, and 875 cm^{-1} for johannite, plášilite, and feynmanite, respectively (Frankland et al., 2022).

256   In general, SO_4^{2-} modes are also distinct when comparing the spectra of these species. Kampf et

257   al. (2019a) assign vibrational modes at 1075, 1042 and 1006 cm^{-1} in feynmanite to v_1 SO_4^{2-}

258   symmetric stretching modes, and similarly, spectral intensities are observed at 1097, 1063, and

259   1029 cm^{-1} in our data for this species. The v_1 SO_4^{2-} modes are observed in plášilite at slightly

260   lower energy than those for feynmanite, with peaks observed at ~1080, 1045, and 1007 cm^{-1}. In

261   johannite, v_1 and v_3 SO_4^{2-} modes are seen at higher energy relative to feynmanite, with bands

262   centered at 1148 and 1045 cm^{-1}, respectively (Frankland et al., 2022; Frost et al., 2005b). A

263   doublet of modes is visible between 1070 and 1115 cm^{-1} in spectra collected for johannite and

264   appears to replace the medium-intensity vibrations observed at 1063 cm^{-1} in plášilite and 1045

265   cm^{-1} in feynmanite. These features may originate from lower space group symmetry in johannite

266   (P-1) relative to plášilite ($P2_1/c$) and feynmanite ($P2/n$). Significant background signal is

267   observed for plášilite and feynmanite, particularly in the low-energy region. It is unclear if this

268   signal indeed originates from these mineral species themselves (e.g., fluorescence) or from

269   matrix material with which they are associated, although optical examination (Figure 5a)

270   suggests that these are pure samples making fluorescence the more likely source of the additional

271   background signal.

272   Below 700 cm^{-1}, spectral complexity is limited for these mineral species. Johannite,

273   plášilite, and feynmanite spectra show bands around 200 cm^{-1} that are attributable to v_2 O–U–O

274   bending modes (Frost et al., 2005b). The multiplicity of features here likely relates to both the

275   number of symmetrically unique O atoms that coordinate U centers and local symmetry

276   constraints of these sites. Between 350 and 400 cm^{-1}, low-intensity modes are observed in the

277   spectra of these 3 species. Based on assignments from Kampf et al. (2019a) for feynmanite, these

278   modes may originate from either U–O equatorial modes or O–M interactions, where M is the

279   charge balancing interstitial species. A few low-intensity peaks are observed between 400 and

280   700 cm^{-1} for johannite, plášilite, and feynmanite, which are assigned to v_4 SO$_4^{2-}$ (~450–490

281   cm^{-1}) and v_2 SO$_4^{2-}$ (~610–650 cm^{-1}).

Chains of Polyhedra

283   Fermiite, meisserite, navrotskyite, and Zn-rich rietveldite (Figure 7a) all contain chains of

284   uranyl pentagonal bipyramidal polyhedra interlinked through sharing of vertices with either four

285   or five SO$_4^{2-}$ tetrahedral units (Figure 7b). Although diversity exists in the position of the v_1

286   UO$_2^{2+}$ mode in spectra for minerals in this group (Figure 8), a few common features are observed

287   between 400 and 700 cm^{-1}. First, spectra for fermiite, navrotskyite, meisserite, and rietveldite all

288   show low-intensity bands between 405 and 480 cm^{-1}, which, based on assignments from Kampf

289   et al. and Plášil et al. (Kampf et al., 2015b; Kampf et al., 2017; Plášil et al., 2013a), can be

290   attributed to v_2 SO$_4^{2-}$ bending modes. Similarly, all species show low-intensity spectral features

291   between ~580 and 675 cm^{-1}, which are assigned as v_4 SO$_4^{2-}$ modes. Significant variability in the

292   position of the v_1 UO$_2^{2+}$ mode is observed, with intensities centered at 824, 847, and 856 cm^{-1}

293   for fermiite, meisserite, and rietveldite, respectively. Two spectra of navrotskyite were collected,

294   and there appears to be variability in the position of the uranyl peak for the 2 data sets, with

295   modes observed at 846 and 850 cm^{-1} for data collected on 2 individual crystals of the same

296   sample. Differences in the SO$_4^{2-}$ region are also observed between the two crystals of the

297   navrotskyite sample we examined. One shows a doublet of modes with a higher-intensity feature

298   centered at 1000 cm^{-1} and a lower-intensity peak at 982 cm^{-1}. The other crystal spectrum shows

299   a triplet of modes with 2 low-intensity peaks at 982 and 1000 cm^{-1} and a more intense peak at

300   1013 cm^{-1}. One of the samples of navrotskyite shows similarity to spectra collected for fermiite.

301   However, optical images of the navrotskyite sample suggest that no additional phases are present

302   (Figure 7a) and may indicate that this phase can either form a solid solution series, be intergrown

303   with a similar, but distinct, mineral species, or possess polarization dependence similar to

304   zippeite group minerals. Additional investigations beyond the scope of this work may prove

305   useful towards determining the origin of spectral signatures we observe for navrotskyite. Of all

306   the uranyl species composed of chains of polyhedra, the sulfate region of fermiite is the most

307   complex with multiple well-resolved bands located between 900 and 1200 cm^{-1}. Although this

308   complexity may originate from four crystallographically distinct S atoms in fermiite, meisserite

309   also possess four unique S sites, and the spectra for this phase are simpler in the sulfate region

310   relative to fermiite. However, comparison of the number of crystallographically unique O sites in

311   fermiite (33) with meisserite (19), suggests that variability in O is the more likely origin of the

312   additional peaks in the 900 to 1200 cm^{-1} region of the spectrum. Of the modes observed in

313   fermiite, 2 are at higher energy relative to other sulfate modes in this group of minerals with

314   peaks seen at ~1070 and 1185 cm^{-1} originating from triply degenerate v_3 SO$_4^{2-}$ vibrations

315   (Kampf et al., 2015b). Meisserite spectra show significant broadening and background

316   contributions below 900 cm^{-1}, perhaps originating from fluorescence of this phase.

Isolated Clusters

318   Belakovskiite, lussierite, and bluelizardite (Figure 9a) are comprised of isolated clusters

319   of uranyl pentagonal bipyramidal polyhedra further coordinated by either four or five sulfate

320   tetrahedra (Figure 9b) and, qualitatively, have greater structural differences between them than

321   other groups of uranyl sulfate minerals discussed in this study so far. Belakovskiite possesses

322   four crystallographically distinct monodentate sulfate tetrahedra bonded to a pentagonal

323   bipyramidally coordinated U center, and an additional sulfate tetrahedra linked only to Na and

324   H_2O. The fifth equatorial O atom coordinating U in this species is an H_2O group (Kampf et al.,

325   2014). Lussierite, also containing U in pentagonal bipyramidal geometry, possesses bidentate

326   coordination in the form of an edge-sharing sulfate group and three additional monodentate

327   sulfate tetrahedra coordinating the U center (Kampf et al., 2019b). The structural unit of

328   bluelizardite is characterized by dimers of uranyl pentagonal bipyramids interconnected by two

329   shared sulfate tetrahedra (Plášil et al., 2014b). Each uranyl center is further coordinated by three

330   additional sulfate groups to form isolated clusters (Figure 9b). These structural differences are

331   manifested in the Raman spectra of these phases (Figure 10). Although the v_1 UO_2^{2+} modes of

332   bluelizardite and belakovskiite appear in similar positions at ~845 cm^{-1}, a significant redshift is

333   observed for the same mode in the spectra of lussierite. The lower energy of the uranyl mode in

334   lussierite is perhaps attributable to weaker U–O_{yl} bond strengths related to the presence of an

335   edge-sharing (rather than vertex sharing) sulfate group. Indeed, bond valence sums provided by

336   Kampf et al. (2019b) indicate that U in lussierite is slightly overbonded (6.10 valence units [vu])

337   with respect to bluelizardite (5.98 vu) (Plášil et al., 2014b). However, more pronounced

338   overbonding is observed for U in belakovskiite (6.22 vu) (Kampf et al., 2014) relative to other

339   uranyl sulfates with structures composed of isolated clusters, suggesting that overbonding is not

340   the origin of the lower energy uranyl signal in lussierite relative to other uranyl sulfates

341   composed of isolated clusters.

342   The sulfate regions of belakovskiite, lussierite, and bluelizardite spectra are complex and

343   highlight the structural information that is extractable from spectroscopic data. In belakovskiite,

344   an intense peak is observed at ~1010 cm^{-1}, with medium- and low-intensity shoulder modes

345   observed at ~980 and 1050 cm^{-1}, respectively. Similarly, an apparent triplet of modes is seen

346   between 970 and 1040 cm^{-1} in bluelizardite. Far more complicated is the region between 920 and

347   1090 cm^{-1} in the spectrum of lussierite, which possesses the largest number (6) (Kampf et al.,

348   2019b) of crystallographically distinct sulfate groups relative to bluelizardite (4) (Plášil et al.,

349   2014b) and belakovskiite (5) (Kampf et al., 2014). Peaks in this region originate from v_1 and v_3

350   SO_4^{2-} modes (Plášil et al., 2014b). The unique equatorial linkages in lussierite and belakovskiite

351   are also reflected in the low-energy regions of the Raman spectra. Only one band is seen for

352   bluelizardite at ~200 cm^{-1} and is assigned to v_2 UO_2^{2+}, 2 modes are observed for belakovskiite

353   and lussierite, with the latter displaying an additional low-energy peak at ~124 cm^{-1}. Similarly, 1

354   v_2 SO_4^{2-} (450 cm^{-1}) mode is observed for bluelizardite, whereas additional modes are seen for

355   other species in this region. Likewise, additional v_4 SO_4^{2-} (~630 cm^{-1}) modes are observed for

356   belakovskiite and lussierite relative to bluelizardite.

357   **Other Uranyl Sulfates: Uranopilite and Ammoniomathesiusite**

358   In addition to uranyl sulfates categorized as belonging to the zippeite or phosphuranylite

359   groups or possessing structures based on chains of polyhedra or isolated clusters, this study also

360   investigates two uranyl sulfate minerals that do not belong to any of those categories. Uranopilite

361   contains dense chains of polyhedra (Burns, 2001; Colmenero et al., 2020), whereas

362   ammoniomathesiusite is a uranyl sulfate vanadate (Kampf et al., 2019c). To investigate unique

363   features in the Raman spectra of these phases, we have compared the Raman spectra for

364   uranopilite and ammoniomathesiusite to average spectra calculated for groups of uranyl sulfate

365   minerals discussed in previous sections.

366   When comparing the Raman spectrum of uranopilite to those of other groups of uranyl

367   sulfate minerals (see Supporting Information, Figure S1), a higher energy v_1 UO_2^{2+} centered at

368   863 cm^{-1} is observed. A unique band centered at 567 cm^{-1} is also seen, which readily

369   distinguishes uranopilite from any other uranyl sulfate phase. The difference is visible because

370   no mode is seen at this frequency in the average spectra of uranyl sulfates belonging to the

371   zippeite group, nor is this mode seen in the average spectra of uranyl sulfates possessing chains

372   of polyhedra or isolated clusters. Based on assignments provided by Frost et al., the band

373   centered at 567 cm^{-1} originates from either v_2 or v_4 SO_4^{2-} bending vibrations. If this mode is

374   indeed a v_2, it occurs at significantly higher energy than the same mode in other uranyl

375   phosphates with structures possessing chains of polyhedra. Likewise, if this mode is a v_4, it is

376   found at significantly lower energy than the same mode in the average spectra of uranyl sulfates

377   with chains of polyhedra. Colmenero et al.(2020) provide a detailed computational investigation

378   of the infrared (IR) spectra of uranopilite using density functional perturbation theory and note

379   several modes in the range of 400-600 cm^{-1}. Unfortunately, we cannot assign our experimental

380   Raman spectra from these computational results without the character of the predicted modes,

381   and thus the ability to discern between Raman and/ or IR active modes. Additional future

382   computational studies may provide clarity as to the identity of this mode.

383   Ammoniomathesiusite possesses square pyramidal vanadyl units in addition to uranyl and

384   sulfate coordination polyhedra. Resultingly, the spectrum of this mineral is distinct from any

385   other group of uranyl sulfate minerals (see Supporting Information, Figure S2). The v_1 UO_2^{2+}

386   mode is centered at 836 cm^{-1} and cannot be used as a diagnostic spectral feature of this phase

387   because this is a similar position observed in other uranyl sulfates. However, 2 higher-energy

388   modes located at ~980 and ~1010 cm^{-1}, attributable to v_1 V–O and S–O modes, respectively, are

389   unique to ammoniomathesiusite relative to uranyl sulfates with other structure types (Kampf et

390   al., 2019c).

391   **Locality Differences: Uranopilite**

392   Frost et al. investigated several samples of uranopilite from varying origins to gain

393   insight into molecular structure variability that may arise from different geochemical settings

394   (Frost et al., 2007). We take a similar approach and compare two data sets for uranopilite and

395   three data sets for natrozippeite from different localities. Spectra for two samples of uranopilite

396   are shown in Figure 11. Data collected for the sample from Apex mine were obtained from

397   RRUFF (Lafuente B, 2015) and were collected with a 780 nm excitation wavelength, whereas

398   the sample from Burro mine studied here was analyzed using a 785 nm laser. Qualitatively, we

399   observe good agreement between the 2 spectra, although data collected with the 780 nm laser

400   appear slightly redshifted compared to our 785 nm data. The v_1 uranyl peak, located at 843 cm^{-1}

401   in the Burro sample, is found at 839 cm^{-1} in the Apex sample. Both spectra appear to possess a

402   shoulder associated with the uranyl band, which may be attributable to slight differences in local

403   coordination environments amongst the six symmetrically distinct U sites (Colmenero et al.,

404   2020). Frost et al. pose that owing to symmetry lowering of the uranyl unit, all uranyl and sulfate

405   vibrational modes are active in both Raman and infrared spectra (Frost et al., 2007). However,

406   we see no such evidence. When bending of the linear axial O–U–O occurs, it is possible that the

407   symmetry-forbidden v_3 UO_2^{2+} mode appears at ~900 cm^{-1} in the Raman resulting from a

408   breakdown of selection rules. However, no peaks are observed in this region for both uranopilite

409   data sets. Slight differences between the position of the v_1 SO_4^{2-} symmetric stretching mode are

410   also observed for the 2 samples, with peaks centered at ~1010 and 1005 cm^{-1} for the Burro and

411   Apex samples, respectively. An apparent triplet of modes is observed at 1097, 1118, and 1145

412   cm^{-1}in the Burro sample, corresponding to the triply degenerate v_3 SO_4^{2-}. Similar features are

413   observed in the spectrum of uranopilite from the Apex mine; however, we provide slightly

414   higher spectral resolution in the data set from Burro. Low-energy modes in the spectra of

415   uranopilite from both samples are in good agreement, but the Burro sample possesses lower

416   background signal, which enables better definition of vibrational modes below 700 cm^{-1}.

417   **Locality Differences: Natrozippeite**

418   Slight differences in spectra for natrozippeite are observed when comparing data sets

419   from different localities (Figure 12). Unlike uranopilite, the v_1 UO_2^{2+} vibrational mode in

420   natrozippeite samples is consistent and appears at 840 cm^{-1} regardless of the locality. All spectra

421   show a low-energy shoulder associated with the uranyl band at ~813 cm^{-1}; however, the

422   spectrum collected for the natrozippeite from the Markey mine appears to have a third low-

423   intensity band located between the 2 uranyl modes at ~825 cm^{-1} (Figure 12a, inset). This

424   difference suggests that additional structural intricacy in the form of an intermediate $U–O_{yl}$ bond

425   distance is present in this sample (Bartlett and Cooney, 1989; Frost et al., 2005a). At 1010 cm^{-1}

426   for all natrozippeite samples, the v_1 SO_4^{2-} symmetric stretching mode is observed. The Blue

427   Lizard and Burro mine natrozippeite appear to have a low-intensity shoulder centered at ~1000

428   cm^{-1}, whereas the Markey mine spectrum shows an additional band at much lower energy, ~975

429   cm^{-1}. This result again suggests that slight structural distortions are present, potentially

430   attributable to variations in locality, and thus, specific geochemical conditions leading to

431   natrozippeite formation (e.g. pH, evaporation rate, etc.). Bands associated with v_3 SO_4^{2-}

432   vibrations are observed at ~1080 and 1090 cm^{-1} for all 3 natrozippeite samples. However, there

433   appears to be some qualitative differences in the line shape of the v_3 SO_4^{2-} bands, which could

434   indicate differences in the static vs. dynamic polarizability of this mode, although the exact

435   origin of these differences is unclear at this time. We also observe a broad band at ~1186 cm^{-1} in

436   the Markey mine sample that is not seen in natrozippeite spectra from other localities.

437   Differences in mineral habit are also observed when comparing three samples of natrozippeite

438   (Figure 12b). The Blue Lizard specimen displays euhedral platy aggregates, and the Markey

439   sample is powdery and cryptocrystalline. Natrozippeite from Burro mine has a somewhat

440   intermediate appearance relative to the other specimens, with small but visible crystallites

441   forming massive aggregates.

Conclusions

443   We have collected Raman spectra for 18 uranyl sulfate minerals after identifying an

444   absence in readily available spectra for these phases. To build a fundamental understanding of

445   common spectral features that relate to uranyl sulfate crystal structures, we present an updated

446   average uranyl sulfate Raman spectrum and suggest potential structural contributions to observed

447   vibrational modes. This study also describes average spectra of groups of uranyl minerals based

448   on structure type. Comparison of spectra within groups of uranyl sulfate minerals based on

449   structure type has also provided insight into the structural origins of observed spectral features,

450   including six members of the zippeite group (including four varieties of natrozippeite), three

451   species with the phosphuranylite anion topology, four minerals composed of chains of polyhedra,

452   three species with structure based on isolated clusters, and two additional uranyl sulfate phases

453   that do not fit into these categories. We have also compared spectra of uranopilite and

454   natrozippeite from different mines and discuss differences therein that could be attributable to

455   their localities of origin.

Implications

457   In the United States and internationally, legacy radionuclide contamination produced

458   during certain stages of the nuclear fuel cycle has had a lasting effect on the environment and

459   will continue to do so for thousands of years. For example, abandoned uranium mines and tailing

460   piles in the western United States have interfaced with meteoric waters for more than 60 years,

461   leading to the migration of uranium and other heavy metals into nearby aquifers, poisoning the

462   wildlife and people who rely on them. The hydration and oxidation processes occurring between

463   primary uranium ores (or wastes) and their host lithologies results in the formation of secondary

464   uranium minerals, including many structurally and chemically complex species new to science.

465   Ultimately, uranium minerals influence the discharge of uranium into the environment. Thus,

466   studying their crystal chemistry and spectroscopy is important, in particular for those species

467   lacking such data, as this study has begun to accomplish.

468   Among secondary uranyl minerals, sulfates are some of the most common alteration

469   products found in U ore deposits and legacy sites related to uranium prospecting, mining, and

470   processing (Gurzhiy and Plášil, 2019; Krivovichev and Plášil, 2013). Uranyl sulfate minerals

471   often occur as admixtures of species, and in some instances, the assemblages are so visually and

472   chemically similar that distinguishing specific species is difficult except by advanced or time-

473   consuming analyses (Frondel, 1958). Despite the many observed commonalities in spectra of

474   uranyl sulfate minerals, we show here that Raman spectroscopy is a powerful means by which to

475   identify underlying structural attributes of a given mineral or group of minerals by comparing the

476   broader species-defining relationships such as topology, interlayer hydrations state, chemistry,

477   and resulting spectroscopic signatures. Given the high structural and chemical diversity of uranyl

478   sulfates attributable to the formation conditions leading to their occurrence (Krivovichev and

479   Plášil, 2013), such rapid and nondestructive identification of uranyl minerals is useful in a broad

480   range of applications.

481   **Acknowledgements**

488   **References**

489   (2021) OriginPro Version2021. OriginLab Corporation, Northampton, MA, USA.

490   Bartlett, J.R., and Cooney, R.P. (1989) On the determination of uranium-oxygen bond lengths in
491   dioxouranium (VI) compounds by Raman spectroscopy. Journal of Molecular Structure,
492   193, 295-300.

493   Brugger, J., Burns, P.C., and Meisser, N. (2003) Contribution to the mineralogy of acid drainage
494   of Uranium minerals: Marecottite and the zippeite-group. American Mineralogist, 88(4),
495   676-685.

496   Burns, P.C. (2001) A new uranyl sulfate chain in the structure of uranopilite. The Canadian
497   Mineralogist, 39(4), 1139-1146.

498   -. (2005) U^{6+} minerals and inorganic compounds: insights into an expanded structural hierarchy
499   of crystal structures. The Canadian Mineralogist, 43(6), 1839-1894.

500   Burns, P.C., Deely, K.M., and Hayden, L.A. (2003) The crystal chemistry of the zippeite group.
501   The Canadian Mineralogist, 41(3), 687-706.

502   Colmenero, F., Plášil, J., Timón, V., and Čejka, J. (2020) Full crystal structure, hydrogen
503   bonding and spectroscopic, mechanical and thermodynamic properties of mineral
504   uranopilite. RSC Advances, 10(53), 31947-31960.

505   Demartin, F., Diella, V., Donzelli, S., Gramaccioli, C., and Pilati, T. (1991) The importance of
506   accurate crystal structure determination of uranium minerals. I. Phosphuranylite
507            $KCa(H_3O)_3(UO_2)_7(PO_4)_4O_4 \cdot 8H_2O$. Acta Crystallographica Section B: Structural Science,
508   47(4), 439-446.

509   Donnay, J. (1955) The primitive cell of johannite. Mineralogical Society of America News and
510   Notes.

511   Finch, R., and Murakami, T. (1999) Systematics and paragenesis of uranium minerals. In P.C.
512   Burns, and R. Finch, Eds. Uranium: Mineralogy, Geochemistry and the Environment 38.
513   Mineralogical Society of America.

514   Frankland, V.L., Milodowski, A.E., and Read, D. (2022) Laser-based characterisation of the
515   copper uranyl sulphate, johannite. Minerals, 12(11), 1419.

516   Frondel, C. (1958) Systematic mineralogy of uranium and thorium. US Government Printing
517   Office.

518 Frost, R., Weier, M., Bostrom, T., Čejka, J., and Martens, W. (2005a) Molecular structure of the
519   uranyl mineral zippeite-An XRD, SEM and Raman spectroscopic study. Neues Jahrbuch
520   fur Mineralogie, Abhandlungen, 181(3), 271-279.
521 Frost, R.L., Čejka, J., Weier, M.L., Martens, W.N., and Ayoko, G.A. (2007) Raman
522   spectroscopy of uranopilite of different origins—implications for molecular structure.
523   Journal of Raman Spectroscopy, 38(4), 398-409.
524 Frost, R.L., Erickson, K.L., Čejka, J., and Reddy, B.J. (2005b) A Raman spectroscopic study of
525   the uranyl sulphate mineral johannite. Spectrochimica Acta Part A: Molecular and
526   Biomolecular Spectroscopy, 61(11-12), 2702-2707.
527 Guettaf, H., Becis, A., Ferhat, K., Hanou, K., Bouchiha, D., Yakoubi, K., and Ferrad, F. (2009)
528   Concentration–purification of uranium from an acid leaching solution. Physics Procedia,
529   2(3), 765-771.
530 Gurzhiy, V.V., and Plášil, J. (2019) Structural complexity of natural uranyl sulfates. Acta
531   Crystallographica Section B: Structural Science, Crystal Engineering and Materials,
532   75(1), 39-48.
533 Kampf, A., Plášil, J., Kasatkin, A., and Marty, J. (2014) Belakovskiite,
534      $Na_7(UO_2)(SO_4)_4(SO_3OH)(H_2O)_3$, a new uranyl sulfate mineral from the Blue Lizard
535   mine, San Juan County, Utah, USA. Mineralogical Magazine, 78(3), 639-649.
536 Kampf, A.R., Kasatkin, A.V., Čejka, J., and Marty, J. (2015a) Plášilite,
537      $Na(UO_2)(SO_4)(OH)•2H_2O$, a new uranyl sulfate mineral from the Blue Lizard mine, San
538   Juan County, Utah, USA. Journal of Geosciences, 60(1), 1-10.
539 Kampf, A.R., Olds, T.A., Plášil, J., and Marty, J. (2023) Zincorietveldite,
540      $Zn(UO2)(SO4)2(H2O)5$, the zinc analogue of rietveldite from the Blue Lizard mine, San
541   Juan County, Utah, USA. Mineralogical Magazine, 1-22.
542 Kampf, A.R., Olds, T.A., Plášil, J., Marty, J., and Perry, S.N. (2019a) Feynmanite, a new sodium
543   uranyl sulfate mineral from Red Canyon, San Juan County, Utah, USA. Mineralogical
544   Magazine, 83(2), 153-160.
545 Kampf, A.R., Olds, T.A., Plášil, J., Nash, B.P., and Marty, J. (2019b) Lussierite, a new sodium
546   uranyl sulfate mineral with bidentate $UO_7–SO_4$ linkage from the Blue Lizard mine, San
547   Juan County, Utah, USA. Mineralogical Magazine, 83(6), 799-808.
548 Kampf, A.R., Plášil, J., Kasatkin, A.V., Marty, J., and Čejka, J. (2015b) Fermiite,
549      $Na_4(UO_2)(SO_4)3• 3H_2O$ and oppenheimerite, $Na_2(UO_2)(SO_4)_2•3H_2O$, two new uranyl
550   sulfate minerals from the Blue Lizard mine, San Juan County, Utah, USA. Mineralogical
551   Magazine, 79(5), 1123-1142.
552 Kampf, A.R., Plášil, J., Nash, B.P., and Marty, J. (2018a) Greenlizardite,(NH4) Na (UO2) 2
553   (SO4) 2 (OH) 2· 4H2O, a new mineral with phosphuranylite-type uranyl sulfate sheets
554   from Red Canyon, San Juan County, Utah, USAANTHONY R. KAMPF ET AL.
555   GREENLIZARDITE, NEW URANYL SULFATE FROM RED CANYON, UTAH.
556   Mineralogical Magazine, 82(2), 401-411.
557 -. (2019c) Ammoniomathesiusite, a new uranyl sulfate–vanadate mineral from the Burro mine,
558   San Miguel County, Colorado, USA. Mineralogical Magazine, 83(1), 115-121.
559 Kampf, A.R., Plášil, J., Olds, T.A., Nash, B.P., and Marty, J. (2018b) Ammoniozippeite, a new
560   uranyl sulfate mineral from the Blue Lizard Mine, San Juan County, Utah, and the Burro
561   Mine, San Miguel County, Colorado, USA. The Canadian Mineralogist, 56(3), 235-245.
562 Kampf, A.R., Sejkora, J., Witzke, T., Plášil, J., Čejka, J., Nash, B.P., and Marty, J. (2017)
563   Rietveldite, $Fe(UO_2)(SO_4)_2(H_2O)_5$, a new uranyl sulfate mineral from Giveaway-Simplot

564   mine (Utah, USA), Willi Agatz mine (Saxony, Germany) and Jachymov (Czech
565   Republic). Journal of Geosciences, 62(2), 107-120.

566 Kohlgruber, T.A., Perry, S.N., Sigmon, G.E., Oliver, A.G., and Burns, P.C. (2022) Hydrogen
567   bond network and bond valence analysis on uranyl sulfate compounds with organic-based
568   interstitial cations. Journal of Solid State Chemistry, 307, 122871.

569 Krivovichev, S.V., and Plášil, J. (2013) Mineralogy and crystallography of uranium. 15-119 p.

570 Lafuente B, D.R.T., Yang H, Stone N. (2015) The power of databases: the RRUFF project.
571   Highlights in Mineralogical Crystallography, p. 1-30. De Gruyter.

572 Ling, J., Sigmon, G.E., Ward, M., Roback, N., and Burns, P.C. (2010) Syntheses, structures, and
573   IR spectroscopic characterization of new uranyl sulfate/selenate 1D-chain, 2D-sheet and
574   3D-framework. Zeitschrift für Kristallographie-Crystalline Materials, 225(6), 230-239.

575 Lu, G., Haes, A.J., and Forbes, T.Z. (2018) Detection and identification of solids, surfaces, and
576   solutions of uranium using vibrational spectroscopy. Coordination chemistry reviews,
577   374, 314-344.

578 Lussier, A.J., Lopez, R.A., and Burns, P.C. (2016) A revised and expanded structure hierarchy of
579   natural and synthetic hexavalent uranium compounds. The Canadian Mineralogist, 54(1),
580   177-283.

581 McDonnell, M., Smith, R., Drane, L., Shields, A., Spano, T., Niedziela, J., Miskowiec, A., and
582   Gibbs, I. (2022) Smart Spectral Matching (SSM). Oak Ridge National Lab.(ORNL), Oak
583   Ridge, TN (United States).

584 Mereiter, K. (1982) The crystal structure of johannite, Cu (UO 2) 2 (OH) 2 (SO 4) 2· 8H 2 O.
585   Tschermaks Mineralogische und Petrographische Mitteilungen, 30, 47-57.

586 Miyawaki, R., Hatert, F., Pasero, M., and Mills, S.J. (2019) New Minerals, Nomenclature and
587   Classification (CNMNC), Newsletter 50. New minerals and nomenclature modifications
588   approved in 2019. Mineralogical Magazine, 83.

589 Plášil, J. (2014) Oxidation-hydration weathering of uraninite: the current state-of-knowledge.
590   Journal of Geosciences, 59(2), 99-114.

591 Plášil, J., Buixaderas, E., Čejka, J., Sejkora, J., Jehlička, J., and Novák, M. (2010) Raman
592   spectroscopic study of the uranyl sulphate mineral zippeite: low wavenumber and U–O
593   stretching regions. Analytical and bioanalytical chemistry, 397(7), 2703-2715.

594 Plášil, J., Dušek, M., Čejka, J., and Sejkora, J. (2014a) The crystal structure of rabejacite, the
595   Ca^{2+}-dominant member of the zippeite group. Mineralogical Magazine, 78(5), 1249-
596   1264.

597 Plášil, J., Kampf, A., Kasatkin, A., Marty, J., Škoda, R., Silva, S., and Čejka, J. (2013a)
598   Meisserite, $Na_5(UO_2)(SO_4)_3(SO_3OH)(H_2O)$, a new uranyl sulfate mineral from the Blue
599   Lizard mine, San Juan County, Utah, USA. Mineralogical Magazine, 77(7), 2975-2988.

600 Plášil, J., Kampf, A.R., Kasatkin, A.V., and Marty, J. (2014b) Bluelizardite, $Na_7(UO_2)(SO_4)$
601        $_4Cl(H_2O)_2$, a new uranyl sulfate mineral from the Blue Lizard mine, San Juan County,
602   Utah, USA. Journal of Geosciences, 59(2), 145-158.

603 Plášil, J., Kasatkin, A., Škoda, R., Novák, M., Kallistová, A., Dušek, M., Skála, R., Fejfarová,
604   K., Čejka, J., and Meisser, N. (2013b) Leydetite, $Fe(UO_2)(SO_4)_2 (H_2O)_{11}$, a new uranyl
605   sulfate mineral from Mas d'Alary, Lodève, France. Mineralogical Magazine, 77(4), 429-
606   441.

607 Plášil, J., Veselovský, F., Hloušek, J., Škoda, R., Novák, M., Sejkora, J., Čejka, J., Škácha, P.,
608   and Kasatkin, A.V. (2014c) Mathesiusite, $K_5(UO_2)_4 (SO_4)_4(VO_5)(H_2O)_4$, a new uranyl

609   vanadate-sulfate from Jáchymov, Czech Republic. American Mineralogist, 99(4), 625-
610   632.
611 Seidel, D. (1981) Extracting uranium from its ores. IAEA Bulletin, 23(2), 24-28.
612 Sharifironizi, M., Szymanowski, J.E., Sigmon, G.E., Navrotsky, A., Fein, J.B., and Burns, P.C.
613   (2016) Thermodynamic studies of zippeite, a uranyl sulfate common in mine wastes.
614   Chemical Geology, 447, 54-58.
615 Smith, P.A., Spano, T.L., and Burns, P.C. (2018) Synthesis and structural characterization of a
616   series of uranyl-betaine coordination complexes. Zeitschrift für Kristallographie-
617   Crystalline Materials, 233(7), 507-513.
618 Spano, T.L., Olds, T.A., McDonnell, M., Smith, R., Niedziela, J.L., Miskowiec, A., Kapsimalis,
619   R., and Shields, A.E. (2023) CURIES: Compendium of Uranium Raman and Infrared
620   Experimental Spectra. American Mineralogist, In Press.
621 Tyumentseva, O.S., Kornyakov, I.V., Britvin, S.N., Zolotarev, A.A., and Gurzhiy, V.V. (2019)
622   Crystallographic insights into uranyl sulfate minerals formation: Synthesis and crystal
623   structures of three novel cesium uranyl sulfates. Crystals, 9(12), 660.

624

625

626

627

628

629

630   **Tables and Figures**
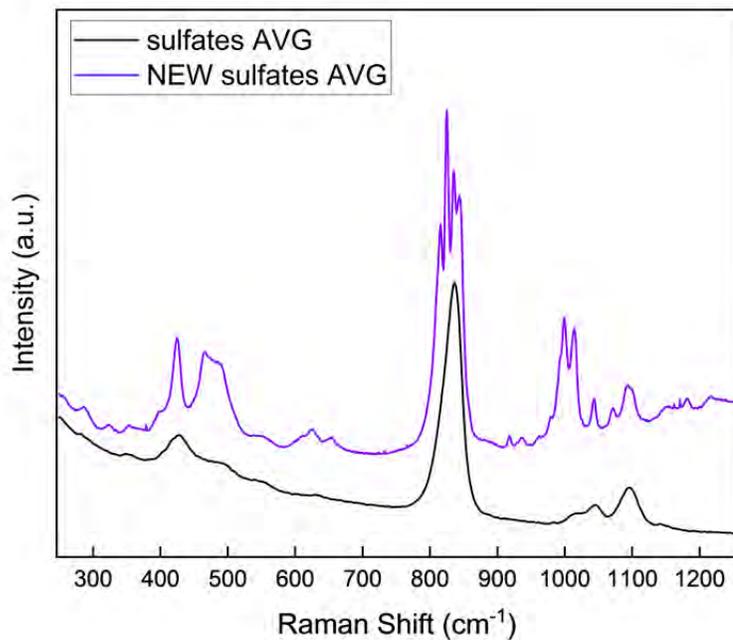
631

632   *Figure 1. Average uranyl sulfate spectra before (black) and after (purple) addition of Raman*
633   *spectra from this work.*
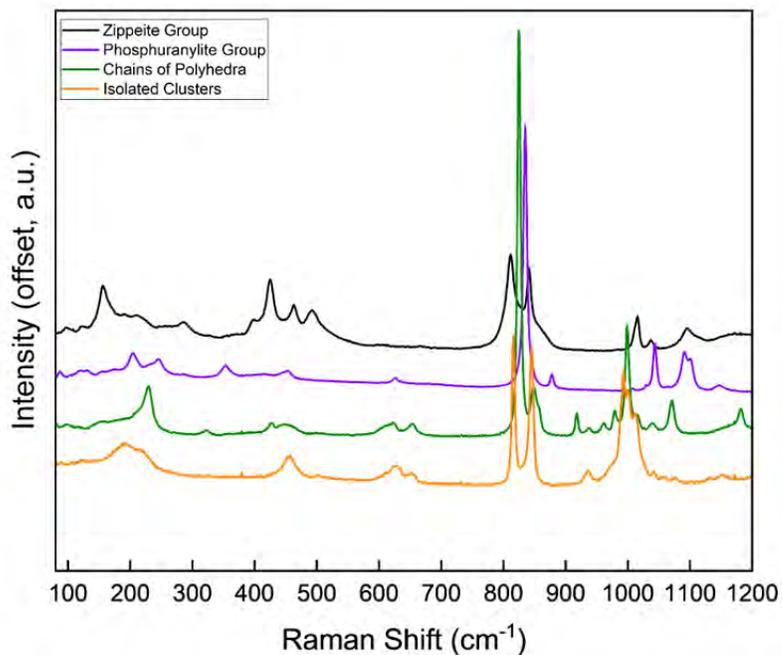
634

635   *Figure 2. Average spectra (offset) for groups of uranyl sulfate minerals based upon structure*
636   *type.*

Table 1. Uranyl sulfate minerals included in this work.

Mineral Name	Structural Unit Type	Anion Topology	Ideal Formula	Space Group	Locality	Sample Description	Reference
Co-rich zippeite	sheet	zippeite	$Co(UO_2)_2(SO_4)O_2 \cdot 3.5H_2O$	$C2/m$	Blue Lizard mine, Red Canyon, UT	Flat orange prisms to ~10 μm	Burns, P. C. et al. 2003
Zn-rich zippeite	sheet	zippeite	$Zn(UO_2)_2(SO_4)O_2 \cdot 3.5H_2O$	$C2/m$	Burro mine, CO	Platy orange crystalline aggregates	Burns, P. C. et al. 2003
uranopilite	chain	dense chains of polyhedra	$(UO_2)_6(SO_4)O_2(OH)_6 \cdot 14H_2O$	$P-1$	Burro mine, CO	Yellow prisms	Burns, P. C. et al. 2001
ammoniozippeite	sheet	zippeite	$(NH_4)_2[(UO_2)_2(SO_4)O_2] \cdot H_2O$	$P4/n$	Burro mine, CO	Thin, flat yellow spear-like crystals	Kampf, A. R. et al. 2018
ammoniomathesiusite	sheet	mathesiusite	$(NH_4)_5(UO_2)_4(SO_4)_4(VO_5) \cdot 4H_2O$	$P4/n$	Burro mine, CO	Yellow-green prisms and powdery aggregates	Kampf, A. R. et al. 2019
natrozippeite	sheet	zippeite	$Na_5(UO_2)_8(SO_4)_4O_5(OH)_3 \cdot 12H_2O$	$P2_1/n$	A: Blue Lizard mine; B: Blue Lizard mine; C: Blue Lizard mine; D: Markey mine, UT; E: Burro mine	A: Yellow blades; B: yellow blades; C: small yellow blades; D: powdery masses; E: powdery masses	Burns, P. C. et al. 2003
johannite	sheet	phosphuranylite	$Cu(UO_2)_2(SO_4)_2(OH)_2 \cdot 8H_2O$	$P-1$	Markey mine, UT	Pale green prisms	Hurlbut, C. S. 1950
marecottite	sheet	zippeite	$Mg_3(UO_2)_8(SO_4)_4O_6(OH)_2 \cdot 28H_2O$	$P-1$	Blue Lizard mine, UT	Orange finely crystalline masses	Brugger, J. et al. 2003
lussierite	clusters	isolated clusters	$Na_{10}[(UO_2)(SO_4)_4](SO_4)_2 \cdot 3H_2O$	Cc	Blue Lizard mine, UT	Small green prisms	Kampf A. R. et al. 2003
zincorietveldite	sheets	chains of polyhedra	$Zn(UO_2)(SO_4)_2(H_2O)_5$	$Pmm2_1$	Giveaway-Simplot mine, UT	Small yellowish-green blades	Kampf A. R. et al. 2022
navrotskyite	chains	chains of polyhedra	$K_2Na_{10}(UO_2)_3(SO_4)_9 \cdot 2H_2O$	$Pbcm$	Blue Lizard mine, UT	Thin, pale-green blades	Olds, T. A. et al. 2019
fermiite	chains	chains of polyhedra	$Na_4(UO_2)(SO_4)_3 \cdot 3H_2O$	$Pmm2_1$	Blue Lizard mine, UT	Aggregate of pale green platy crystals	Kampf, A. R., et al. 2015
belakovskiite	clusters	isolated clusters	$Na_7(UO_2)(SO_4)_4(SO_3OH)(H_2O)_3$	$P-1$	Blue Lizard mine, UT	Finely fibrous pale-green needles on gyspum	Kampf, A. R., et al. 2014
plásilite	sheet	phosphuranylite	$Na(UO_2)(SO_4)(OH) \cdot 2H_2O$	$P2_1/c$	Blue Lizard mine, UT	Thin green prisms	Kampf. A. R., et al. 2015
feynmanite	sheet	phosphuranylite	$Na(UO_2)(SO_4)(OH) \cdot 3.5H_2O$	$P2/n$	Markey mine, UT	Thin pale-green prisms	Kampf, A. R., et al. 2019
bluelizardite	isolated clusters	isolated clusters	$Na_7(UO_2)(SO_4)_4Cl \cdot H_2O$	$C2/c$	Blue Lizard mine, UT	Thin, stubby green prisms	Plásil, J., et al. 2014
meisserite	chains	chains of polyhedra	$Na_5(UO_2)(SO_4)_3(SO_3OH)(H_2O)$	$P-1$	Blue Lizard mine, UT	Anhedral green masses on gypsum	Plásil, J., et al. 2013
rabejacite	sheet	zippeite	$Ca(UO_2)_4(SO_4)_2(OH)_6 \cdot 6H_2O$	$P-1$	Blue Lizard mine, UT	Small yellow plates	Plásil, J., et al. 2018

637

638   *Table 2. Assignment of features in the average Raman spectra for uranyl sulfate mineral groups*

| Feature (cm^{-1})	Structure Type	Assignment	Reference
157	zippeite	U-O equatorial modes	Plášil et al., 2010
~380-550	zippeite	$v_2UO_2^{2+}$, $v_3SO_4^{2-}$, U-O equatorial modes	Plášil et al., 2010; Frost et al., 2005a
810, 840	zippeite	$v_1UO_2^{2+}$	Plášil et al., 2010; Frost et al., 2005a
1015	zippeite	$v_1SO_4^{2-}$	Plášil et al., 2010
1095	zippeite	$v_3\,SO_4^{2-}$	Plášil et al., 2010
~190-260	phosphuranylite	$v_2UO_2^{2+}$	Kampf et al., 2019a; Frost et al., 2005b
350	phosphuranylite	U-O equatorial modes, or O-M[§] interactions	Kampf et al., 2019a; Kampf et al., 2018a
450	phosphuranylite	$v_2SO_4^{2-}$	Kampf et al., 2019a; Kampf et al., 2018a
625	phosphuranylite	$v_4SO_4^{2-}$	Kampf et al., 2019a; Kampf et al., 2018a
834, 875	phosphuranylite	$v_1UO_2^{2+}$	Frankland et al., 2022
1045-1115	phosphuranylite	$v_1SO_4^{2-}$, $v_3\,SO_4^{2-}$	Frankland et al., 2022; Frost et al., 2005b
230	chains of polyhedra	$v_2UO_2^{2+}$	Kampf et al., 2015b
~405-480	chains of polyhedra	$v_2SO_4^{2-}$	Kampf et al., 2015b; Kampf et al., 2017; Plášil et al., 2013a
~580-675	chains of polyhedra	$v_4SO_4^{2-}$	Kampf et al., 2015b; Kampf et al., 2017; Plášil et al., 2013a
824, ~840-860	chains of polyhedra	$v_1UO_2^{2+}$	Kampf et al., 2015b; Kampf et al., 2017; Plášil et al., 2013a
~900-1085	chains of polyhedra	$v_3\,SO_4^{2-}$	Kampf et al., 2015b; Kampf et al., 2017; Plášil et al., 2013a
~150-250	isolated clusters	$v_2UO_2^{2+}$	Kampf et al., 2019b
455	isolated clusters	$v_2\,SO_4^{2-}$	Kampf et al., 2019b
~595-670	isolated clusters	$v_4\,SO_4^{2-}$	Plášil et al., 2014b; Kampf et al., 2019b, Kampf et al., 2014
815, 845	isolated clusters	$v_1UO_2^{2+}$	Plášil et al., 2014b; Kampf et al., 2019b, Kampf et al., 2014
935, ~950-1080	isolated clusters	$v_1,v_3\,SO_4^{2-}$	Plášil et al., 2014b; Kampf et al., 2019b

[§]M = charge balancing species

639

640
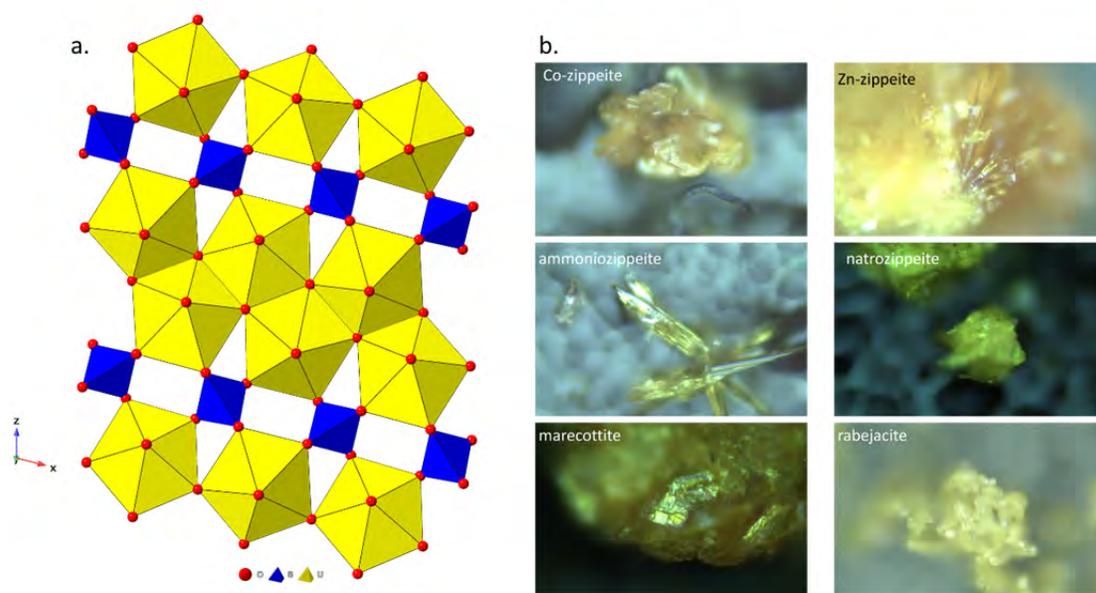
Figure 3. a. The structural unit of minerals possessing the zippeite anion topology. b. Zippeite group minerals investigated in this work. Horizontal field of view for all sample photographs is 450 μm.


644
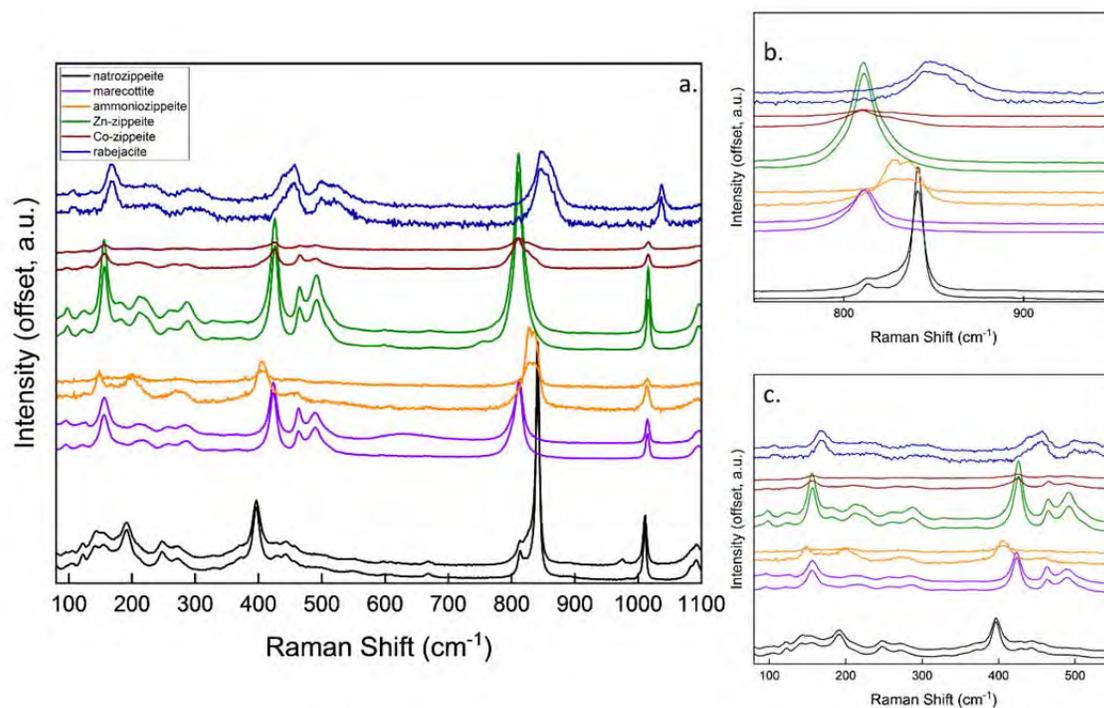
Figure 4.a. Spectra (offset) for several uranyl sulfate minerals that possess the zippeite anion topology. For simplicity, two datasets are shown for each species and additional datasets collected for zippeite group minerals are included in Supporting Information. b. The uranyl

648 *region of zippeite group uranyl sulfate spectra (offset). c. The low energy region of zippeite*
649 *group uranyl sulfate spectra (offset).*
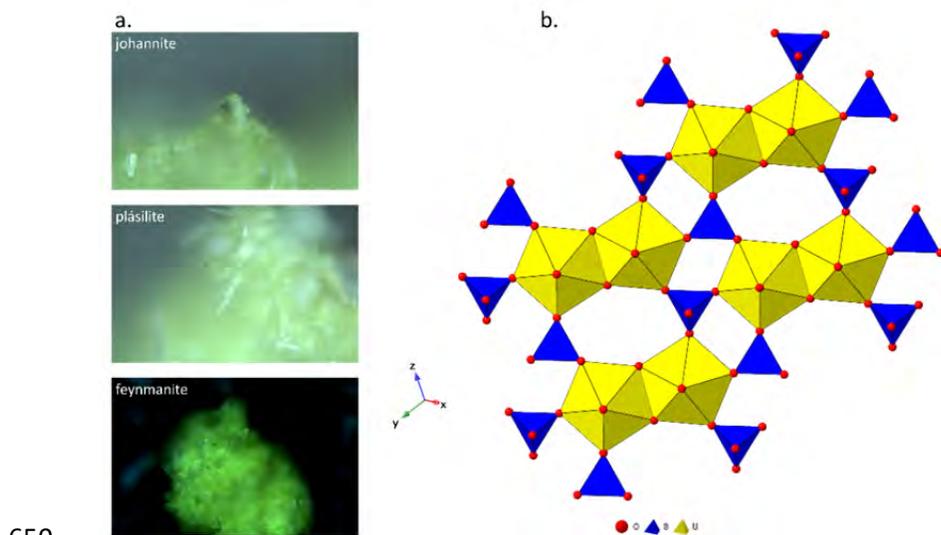
650

651 *Figure 5. a. Phosphuranylite group minerals investigated in this work. Horizontal field of view*
652 *for all sample photographs is 450 μm. b. The phosphuranylite anion topology as seen in*
653 *johannite.*
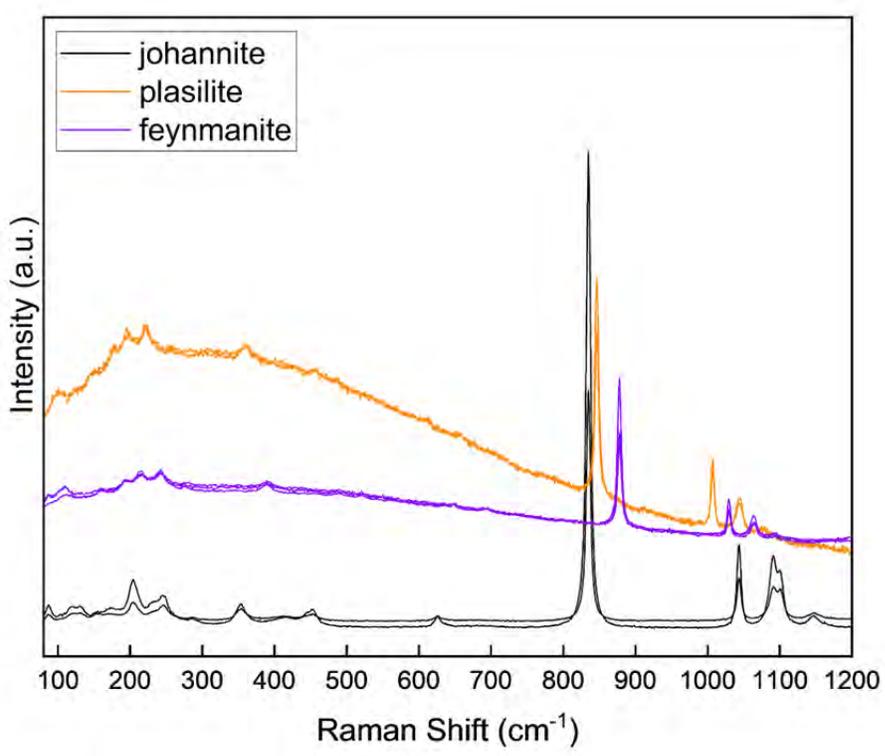
654

655 *Figure 6. Spectra for uranyl sulfate minerals that possess the phosphuranylite anion topology.*

656
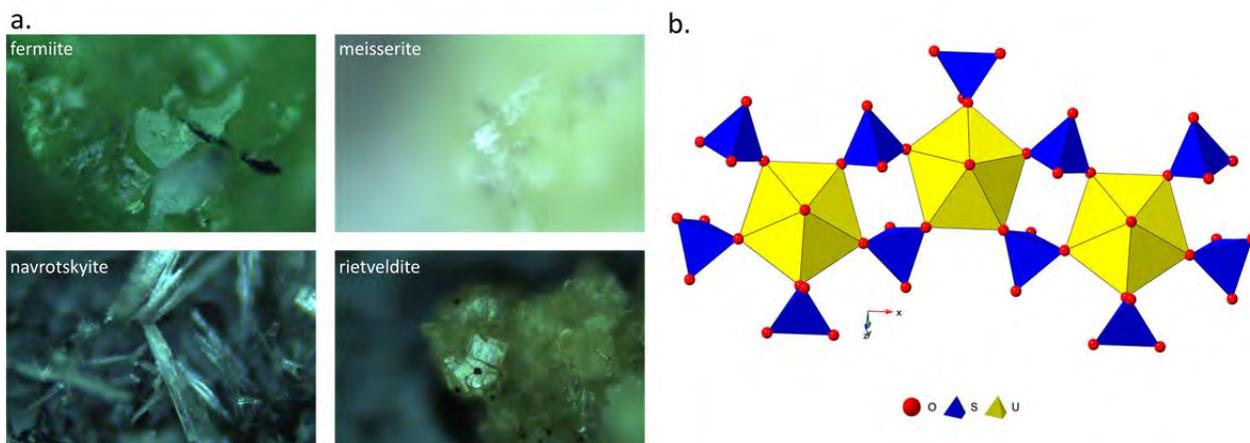
Figure 7 a. Uranyl sulfate minerals investigated in this work that contain chains of polyhedra, such as fermiite (b). Horizontal field of view for all sample photographs is 450 μm.

659

660
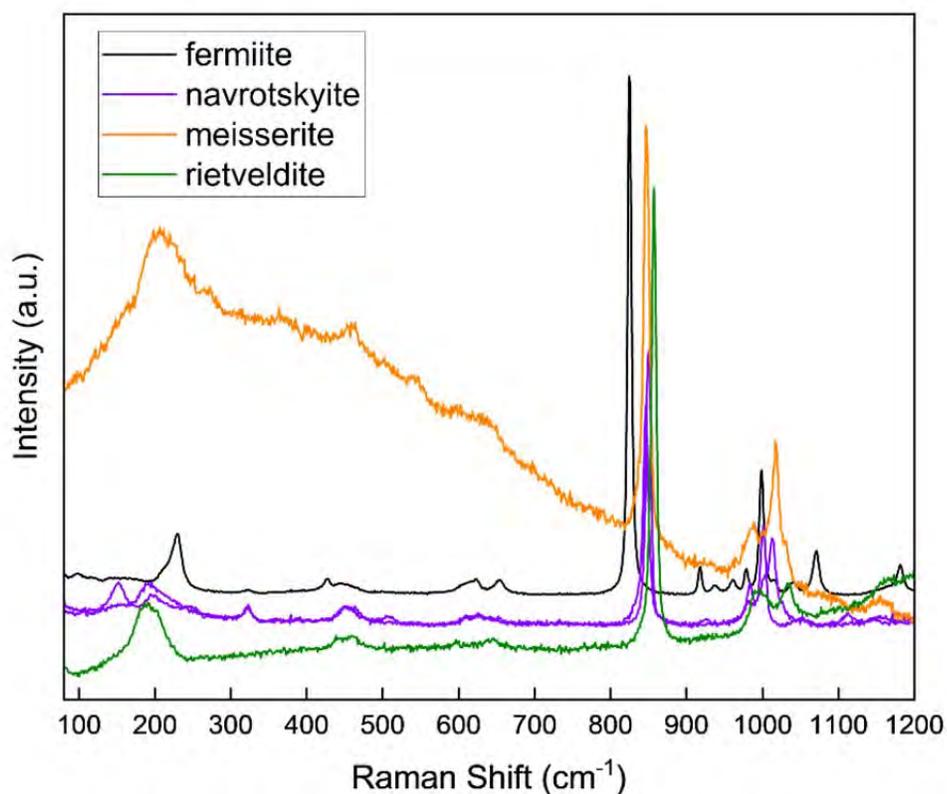
*Figure 8. Raman spectra collected for uranyl sulfate minerals composed of chains of polyhedra.*
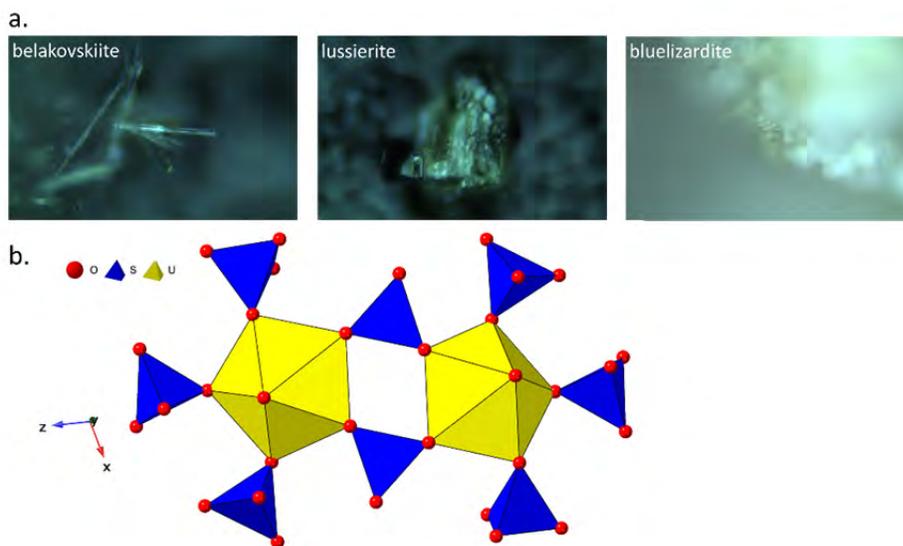
662

663   *Figure 9. a. Uranyl sulfate minerals composed of isolated clusters such as bluelizardite (b.).*
664   *Horizontal field of view for all sample photographs is 450 μm.*
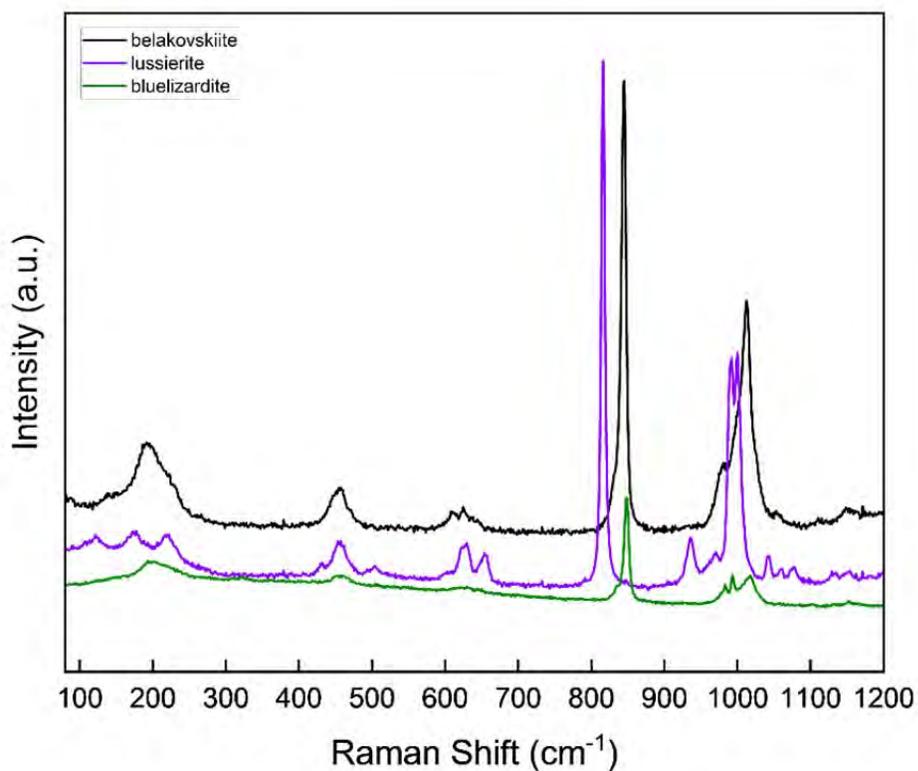
665

666   *Figure 10. Raman spectra collected for uranyl sulfate minerals composed of isolated clusters.*

667
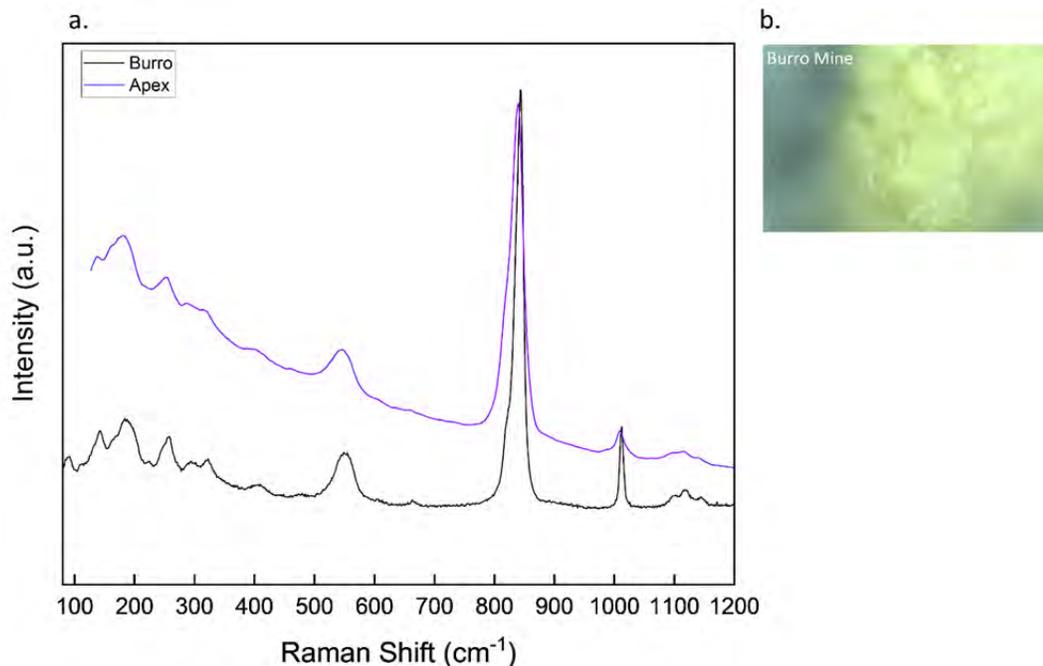
Figure 11. a. Comparison of Raman spectra collected for uranopilite (b.) in this work, and published data. Horizontal field of view for all sample photographs is 450 μm.

668
669

670
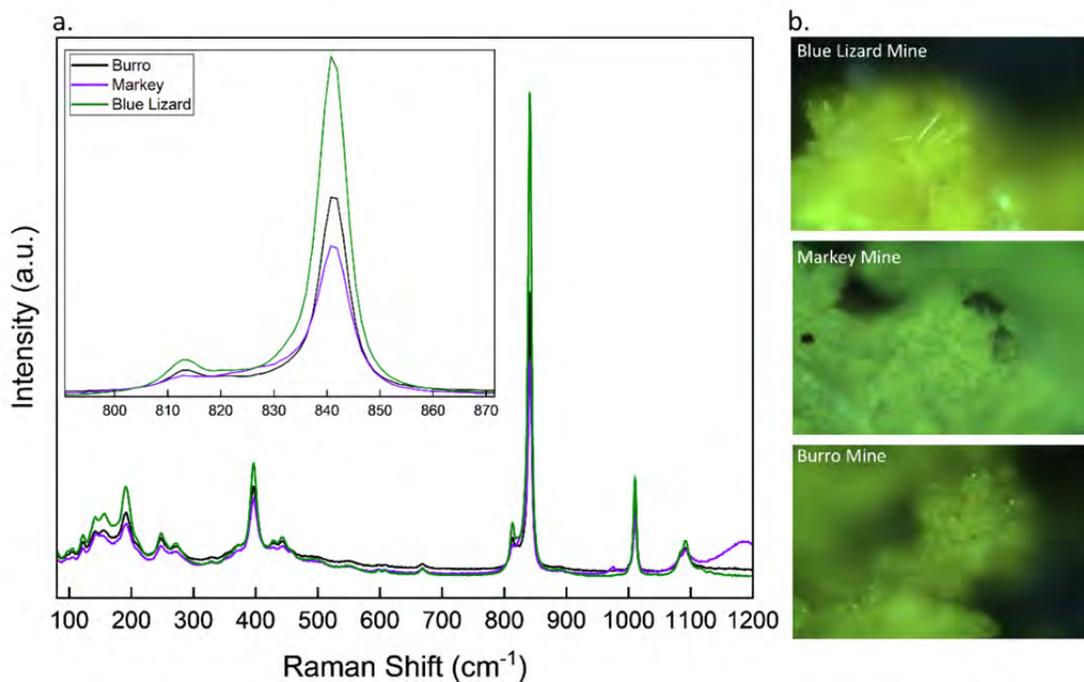
Figure 12 a. Comparison of Raman spectra collected for natrozippeite (b.) for several localities. Horizontal field of view for all sample photographs is 450 μm.

671
672